

Cluster-Containing MOFs

 International Edition: DOI: 10.1002/anie.201907136
 German Edition: DOI: 10.1002/ange.201907136

Bi-Microporous Metal–Organic Frameworks with Cubane $[M_4(OH)_4]$ ($M = Ni, Co$) Clusters and Pore-Space Partition for Electrocatalytic Methanol Oxidation Reaction

 Ya-Pan Wu⁺, Jun-Wu Tian⁺, Shan Liu, Bo Li, Jun Zhao, Lu-Fang Ma, Dong-Sheng Li,* Ya-Qian Lan, and Xianhui Bu*

Abstract: Embedding cubane $[M_4(OH)_4]$ ($M = Ni, Co$) clusters within the matrix of metal–organic frameworks (MOFs) is a strategy to develop materials with unprecedented synergistic properties. Herein, a new material type based on the pore-space partition of the cubic primitive minimal-surface net (MOF-14-type) has been realized. CTGU-15 made from the $[Ni_4(OH)_4]$ cluster not only has very high BET surface area ($3537\text{ m}^2\text{ g}^{-1}$), but also exhibits bi-microporous features with well-defined micropores at 0.86 nm and 1.51 nm. Furthermore, CTGU-15 is stable even under high pH (0.1 M KOH), making it well suited for methanol oxidation in basic medium. The optimal hybrid catalyst KB&CTGU-15 (1:2) made from ketjen black (KB) and CTGU-15 exhibits an outstanding performance with a high mass specific peak current of 527 mA mg^{-1} and excellent peak current density (29.8 mA cm^{-2}) at low potential (0.6 V). The isostructural cobalt structure (CTGU-16) has also been synthesized, further expanding the application potential of this material type.

Direct methanol fuel cells (DMFCs), with high energy conversion efficiency and low operating temperature, have attracted extensive attention as a green carbon-neutral technology to meet the growing energy demand.^[1] However, the anode kinetics of the methanol oxidation reaction (MOR) are sluggish, creating an essential need for better electro-

catalysts to enhance the performance of DMFCs.^[2] Although great progress has been made towards the development of non-precious-metal-based catalysts, Pd- or Pt-based materials are still well-recognized high-efficiency electrocatalysts for methanol electro-oxidation. But the high cost and limited supply of platinum and palladium deter the large-scale commercial development of DMFCs.^[3] One key issue for DMFC technology is the fabrication of cost-effective and high-efficiency electrocatalysts for the anodic methanol oxidation reaction.^[4] Therefore, the search for efficient, durable, and inexpensive alternatives to Pt-based catalysts is of utmost importance. Although Ni-based nanomaterials^[5] such as NiO ,^[6] $Ni(OH)_2$,^[7] nickel layered double hydroxide ($Ni-LDH$),^[8] and $PtNi$ ^[9] and $NiCu$ ^[10] alloy particles have been studied as promising candidates for electrochemical MOR, the tendency for nanoparticles to aggregate and the deactivation by harmful intermediates are factors limiting their applications.

Metal–organic frameworks (MOFs), with their unique properties and large surface areas, have been extensively explored as promising electrocatalysts.^[11] The integration of diverse active units such as titanium oxide clusters,^[12] zirconium oxygen clusters,^[13] polyoxometalates,^[14] and transition metal oxygen clusters^[15] into MOFs can remarkably enhance their activities for catalysis. As secondary building units for MOFs, square-planar, Zn_4O -type, and cubane-type tetranuclear clusters have drawn extensive interest. The classical square-planar M_4 units^[16] and Zn_4O -type clusters^[17] are very common. In comparison, MOFs based on cubane $[M_4(OH)_4]$ clusters are rare. Recently, clusters such as $[Co_4O_4]$,^[18] $[MnCo_3O_4]$,^[19] $[Mn_4CaO_4]$,^[20] $[(Co/Fe)_4O_4]$ ^[21] have been used as catalysts for photosynthesis and electrocatalytic water splitting. Although various structural mimics of the electrocatalysts have been reported,^[22] cubane $[Ni_4(OH)_4]$ cluster-based porous MOFs as an anode electrocatalyst for MOR have been rarely studied.

Similar to the well-known 6-connected $[Zn_4O]^{6+}$ cluster found in MOF-5, $[Ni_4(OH)_4]^{4+}$ also has six symmetrically equivalent edges defined by two adjacent metal sites at the vertices of the M_4 metal tetrahedron. Thus, in principle, new $[Ni_4(OH)_4]^{4+}$ structures can be created by re-imagining the existing library of $[Zn_4O]^{6+}$ structures. A challenge is that while both $[Zn_4O]^{6+}$ and $[Ni_4(OH)_4]^{4+}$ can act as 6-connected nodes, $[Ni_4(OH)_4]^{4+}$ has a lower positive charge than $[Zn_4O]^{6+}$ so that ligands or ligand combinations effective in $[Zn_4O]^{6+}$ structures may not work with $[Ni_4(OH)_4]^{4+}$. To address this challenge, our synthetic strategy explores the use of -3

[*] Dr. Y.-P. Wu,^[†] J.-W. Tian,^[†] S. Liu, B. Li, Prof. Dr. J. Zhao, Prof. Dr. D.-S. Li
 College of Materials and Chemical Engineering
 Key Laboratory of Inorganic Nonmetallic Crystalline and Energy Conversion Materials, China Three Gorges University
 Yichang 443002 (China)
 E-mail: lidongsheng1@126.com

Prof. Dr. L.-F. Ma
 College of Chemistry and Chemical Engineering
 Luoyang Normal University, Luoyang 471934 (China)
 Prof. Dr. Y.-Q. Lan
 School of Chemistry and Materials Science
 Nanjing Normal University, Nanjing 210023 (China)

Prof. Dr. X. Bu
 Department of Chemistry and Biochemistry
 California State University, Long Beach
 1250 Bellflower Boulevard, Long Beach, CA 90840 (USA)
 E-mail: xianhui.bu@csulb.edu

[†] These authors contributed equally to this work.

Supporting information and the ORCID identification number(s) for the author(s) of this article can be found under:
<https://doi.org/10.1002/anie.201907136>.

tricarboxylate ligands with neutral bipyridyl ligands, which ideally solve this issue.

Herein, we have synthesized and structurally characterized a Ni-based highly porous 3D MOF, $[\text{Ni}_4(\text{OH})_4(\text{TATB})_{4/3}(\text{BPE})_2]$ (CTGU-15; $\text{TATB} = 4,4',4''\text{-s-triazine-2,4,6-tribenzoic acid}$, $\text{BPE} = \text{trans-1,2-bis(4-pyridyl)ethylene}$), containing cubane $[\text{Ni}_4(\text{OH})_4]$ clusters and a $-3/0$ ligand combination. Green polyhedral-shaped crystals of CTGU-15 were obtained by solvothermal synthesis of $\text{Ni}(\text{ClO}_4)_2 \cdot 6\text{H}_2\text{O}$ with TATB and BPE in DMA/ H_2O solution with HBF_4 as an additive at 120°C for 24 h. A similar synthetic strategy was used to obtain a cobalt MOF (denoted CTGU-16; Table S1). Since CTGU-16 is isostructural to CTGU-15, the structure and properties of CTGU-15 are described below.

CTGU-15 can be visualized as a pore-space-partitioned $\text{Cu}_2\text{-BTB}$ -based MOF-14 framework, and alternatively as a nitrogen-rich, $\text{Ni}_4(\text{OH})_4$ variant of a $\text{Zn}_4\text{O-BTB-2,6-NDC}$ -based DUT-6/MOF-205 framework ($\text{H}_3\text{BTB} = 1,3,5\text{-tris(4-carboxyphenyl)benzene}$, $2,6\text{-NDC} = 2,6\text{-naphthalene-dicarboxylate}$).^[23] In MOF-14, square-planar Cu_2 paddlewheel clusters are joined by BTB into a (3,4)-connected interpenetrating Pt_3O_4 -type net. In non-interpenetrated DUT-6 and MOF-205, the Zn_4O cluster mimics the Cu_2 square-planar pattern with four of its six tetrahedral edges. The remaining two opposite edges of each Zn_4O cluster are further bridged to adjacent clusters by dicarboxylate ligands (i.e., 2,6-NDC). In CTGU-15, $[\text{Ni}_4(\text{OH})_4]$ clusters mimic Zn_4O clusters with four of its six tetrahedral edges. However, due to lower charge on the $[\text{Ni}_4(\text{OH})_4]$ cluster and the four available Ni coordination sites, two neutral BPE ligands act in tandem to bridge two adjacent $[\text{Ni}_4(\text{OH})_4]$ clusters. Therefore, unlike the well-known *pacs* system,^[24] in which the pore-partition agent is a single tpt ligand (tpt = 2,4,6-tris(4-pyridyl)-1,3,5-triazine), the pore-partition agent in CTGU-15 consists of a ligand pair (two BPE ligands). Pore space partition (PSP) has been reported as a powerful tool in property engineering on the *pacs* platform which is based on trimeric $\text{M}_3(\text{OH})_3/\text{O}$ clusters. The extension here to $\text{Ni}_4(\text{OH})_4$ cubane clusters and the double-ligand mode represents a major advance. One advantage of the double-ligand pore-space-partition mode is apparently high stability, as observed in CTGU-15, which is particularly desirable for electrocatalytic applications which often require relatively harsh conditions (as compared to gas storage and separation applications). The integration of CTGU-15 and ketjen black (KB) generates a series of MOF-based composites KB&CTGU-15 which are effective electrocatalysts for the methanol oxidation reaction. The optimal catalyst KB&CTGU-15(1:2) shows a much enhanced efficiency.

X-ray structure analysis reveals that CTGU-15 crystallizes in the cubic $Pm\bar{3}n$ space group, showing a 3D neutral porous framework with cubane $[\text{Ni}_4(\text{OH})_4]$ as the building unit (Figure S5a). The Ni1 center is six-coordinated by two carboxylate O atoms and one BPE N atom, and three $\mu_3\text{-OH}$ O atoms in a distorted octahedral $[\text{NiO}_5\text{N}]$ geometry (Figure S2). It is noteworthy that four symmetry-related Ni1 atoms are bridged by four $\mu_3\text{-OH}$ O atoms to afford a cubane $[\text{Ni}_4(\text{OH})_4]$ cluster (Figure 1a, Figure S3).

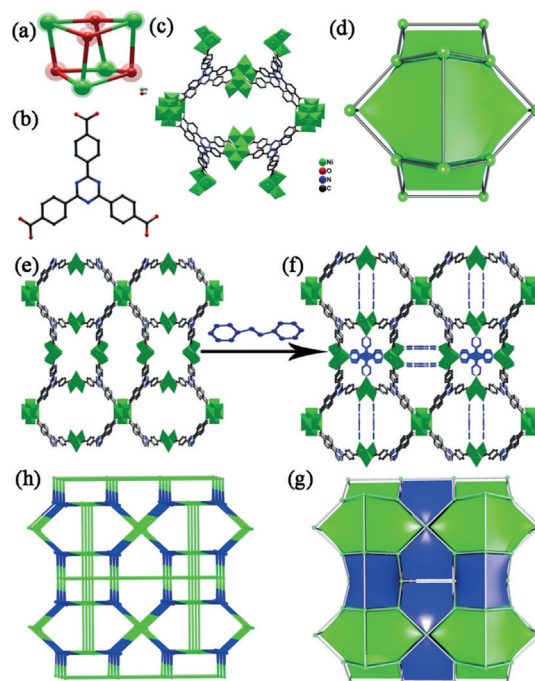


Figure 1. Pore-space partition of the highly symmetrical (3,4)-connected net in CTGU-15: (a) The cuboidal $[\text{Ni}_4\text{O}_4]$ subunit; (b) the TATB molecule; (c,d) the (3,4)-connected Pt_3O_4 -type net formed from $[\text{Ni}_4\text{O}_4]$ cubane and TATB ligands and the tiling illustration; (e,f) pore-space partition through symmetry- and size-matching-regulated double BPE insertion; (g,h) the (3,6)-c *ith-d* net topology and tiling diagram.

Interestingly, cubane $[\text{Ni}_4(\text{OH})_4]$ units are linked by TATB ligands (Figure 1b) to generate a porous net similar to MOF-14 based on 4-connected Cu_2 and 3-connected BTB ligands (Figure 1c,d). As a result, an extended 3D network with 1D nanosized hexagon and square channels running along the $[100]$ direction was formed (Figure 1e). Simultaneously, the original 1D channels along the crystallographic c axis (with an aperture size of $13.4 \times 27.3 \text{ \AA}^2$ and $13.4 \times 13.4 \text{ \AA}^2$) (Figure S4) are embedded by the BPE pore-partitioning ligands with parallel and vertical modes (at an interval of ca. 9.3 \AA) into numerous uniform interconnected pore cavities (Figure 1f).^[25] Noteworthy is that although the $[\text{Ni}_4(\text{OH})_4]$ clusters are known, the integration of this cubane cluster into a 3D metal-organic framework is unusual (Figure S5a). Topologically, if the TATB ligand and the $[\text{Ni}_4(\text{OH})_4]$ unit are simplified as 3- and 6-c nodes, respectively, then the 3D framework of CTGU-15 exhibits a (3,6)-connected *ith-d* network with a point symbol of $(5^{12}8^3)(5^3)_4$ (Figure 1g,h and Figure S5b). The total guest-accessible volume in CTGU-15 is very high, reaching as much as 79.2%, as calculated by PLATON. Obviously, even after the pore-space partition (PSP) approach, the pore volume is still larger than that of many other highly microporous MOFs. The high surface area and relatively large pore size (Figure S9) are expected to facilitate the adsorption/diffusion of reaction species and enhance the electrocatalytic activity.

The characteristic powder X-ray diffraction (PXRD) peaks of CTGU-15 match well with the simulated ones from single-crystal X-ray diffraction (Figure S6), confirming

its good crystallinity and high purity. To assess the chemical durability of CTGU-15 in electrolyte solution, 100 mg of crystalline sample was immersed in 20 mL 0.1 M KOH at room temperature, the PXRD patterns remain unchanged after 24 h (Figure S6). These results confirm the excellent stability of CTGU-15 in 0.1 M KOH and indicate its potential as a MOR electrocatalyst in alkaline medium.

The MOR catalytic activity of CTGU-15 was initially recorded at a scan rate of 50 mV s^{-1} in N_2 -purged 0.1 M KOH solution with and without 1.0 M methanol (Figure S11). In order to eliminate the double-layer capacitor effect, all obtained data are normalized to mass activity. It is noted that the anodic current density increases sharply after addition of methanol, revealing the obvious electrochemical response of CTGU-15 for methanol oxidation (Figure S11 a). When measured in solutions containing 0.1 M KOH with 1.0 M CH_3OH at different scan rates, the current density of CTGU-15 increases with the increase of scan rate (Figure S11 b). And the peak current densities increase linearly with the square root of the scan rate for sweep rates from 10 to 50 mV s^{-1} as expected (Figure S11 c). Such a response is attributed to the electrochemical activity of the redox couple over the surface that is enhanced with the speed of reaction.

Apart from catalytic mass activity, methanol concentration is another index to assess MOR performance. Methanol-concentration-dependent cyclic voltammetry (CV) was performed with CTGU-15 catalyst in 0.1 M KOH with different concentrations of methanol (0.5, 1.0, 2.0, 3.0 M CH_3OH). The peak current density increases linearly with methanol concentration from 0.5 to 1.0 M, revealing that the diffusion of the reaction species plays a vital role in the rate-limiting step. When the concentration of methanol surpasses 2.0 M, the oxidation peak current density remains constant, suggesting that the rate-determining step has changed to a reaction-kinetics-controlled process and is largely resolved by the catalytic reaction rate at the electrode interface (Figure S12, Table S4). As we know, most Ni-based catalysts have been reported using lower concentrations of methanol, ranging from 0.5 to 2.0 M. For CTGU-15, the mass activity and peak current density of CTGU-15 catalyst in 1.0 M CH_3OH is greater than that at other concentrations of methanol (0.5, 2.0, and 3.0 M).

In order to further clarify the factors contributing to the MOR activity of CTGU-15, the CV curves for activating catalysts and MOR in 0.1 M KOH and 0.1 M KOH + 1.0 M CH_3OH were generated for KB&CTGU-15 hybrid samples and pure CTGU-15 (Figure 2a,b, Figures S13–S16). As shown in Figure 2a, five electrocatalysts exhibit typical CV behavior in 0.1 M KOH solution at a scan rate of 50 mV s^{-1} . The peaks are anodic and cathodic at around 0.55 V and 0.45 V, respectively, corresponding to the conversion of Ni^{II} to Ni^{III} during the catalyst activation. The peaks centered at around 0.8 V are undoubtedly due to MOR. Judging from the mass-specific current density in the forward scan, the KB&CTGU-15(1:2) hybrid sample exhibits the highest MOR activity (527 mA mg^{-1}), which is larger than those of KB&CTGU-15(1:1) (456 mA mg^{-1}), KB&CTGU-15(1:3) (495 mA mg^{-1}), and KB&CTGU-15(1:4) (483 mA mg^{-1}), and around 2.5 times higher than that of pure CTGU-15 (203 mA mg^{-1})

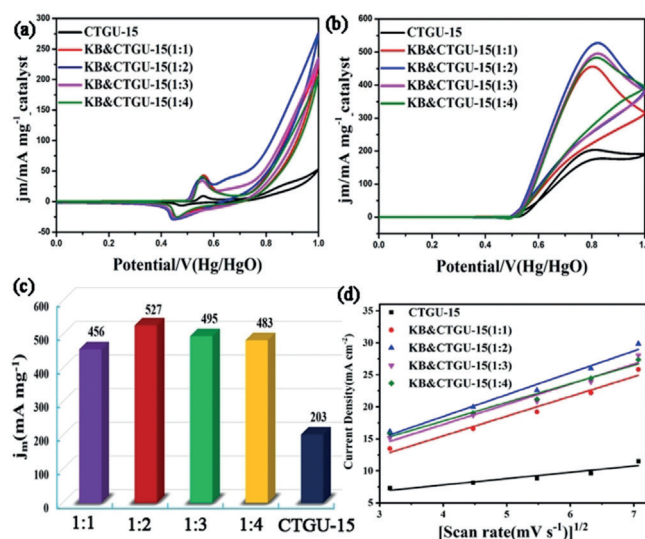


Figure 2. (a) Mass-normalized CV curves of different catalysts in 0.1 M KOH recorded at a scan rate of 50 mV s^{-1} . (b) CV curves of catalysts for CH_3OH electro-oxidation in 0.1 M KOH with 1.0 M methanol. (c) Bar graph of the mass activities of various catalysts. (d) The linear relationship between the current density and the square root of the scan rate for various catalysts.

(Figure 2c). The peak current density of KB&CTGU-15(1:2) attains 29.8 mA cm^{-2} at a potential of 0.6 V, which is higher than those of other catalysts at the same potential (Table S3). The improved activity of the KB&CTGU-15(1:2) hybrid suggests a lower activation energy for MOR in the presence of moderate KB. Furthermore, as shown in Figure 2d, there is a linear relationship between the current densities and the square root of the scan rate for different catalysts, implying that the oxidation of methanol is determined by its diffusion speed. In order to confirm the difference in MOR performance of the double-ligand PSP material (CTGU-15) and single-ligand PSP material, a well-known single-ligand pore-space partitioned material (CPM-33a) was prepared according to the literature.^[26] The PXRD of the as-synthesized sample matches well with the simulated one (Figure S17). The MOR activities of CPM-33a and CTGU-15 were evaluated under the same testing conditions; the mass-normalized CV and CH_3OH electro-oxidation curves are shown in Figure S18. CPM-33a sustains a mass peak current density of 110 mA mg^{-1} and specific area activity (12.5 mA cm^{-2}). The MOR performance of CTGU-15 is superior to that of CPM-33a, which might be attributed to more efficient electron transport and electrolyte entrance between cubane $[\text{Ni}_4(\text{OH})_4]$ units and the higher BET surface area of CTGU-15. A comparison of the catalytic properties of CTGU-15, its hybrid catalysts, and known MOR catalysts is given in Table S5.

The morphology and microstructure of KB&CTGU-15-(1:2) were studied further (Figure 3). The slice structure of the hybrid sample is clearly confirmed by transmission electron microscopy (Figure 3b,d). Energy-dispersive spectroscopy (EDS) mapping shows that elemental Ni, C, N and O are distributed uniformly in the composites and that ketjen black particles decorate the surface of CTGU-15. Also, the survey

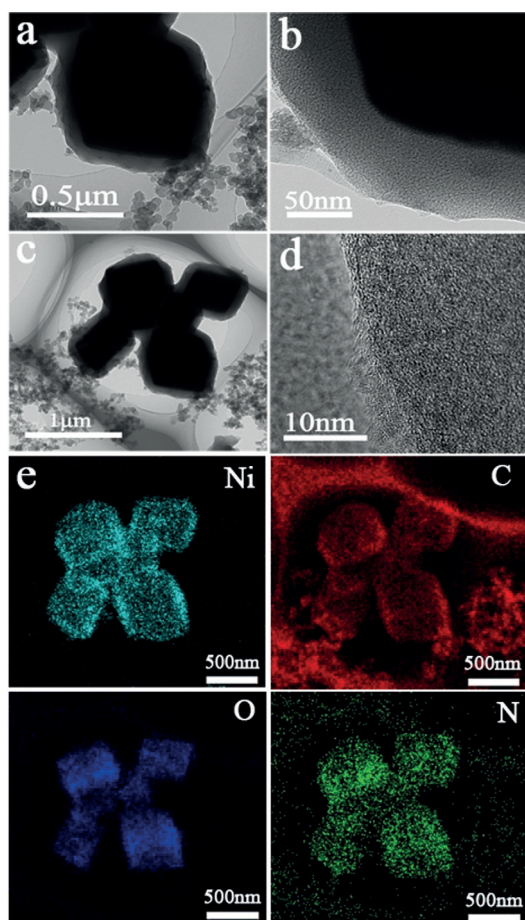


Figure 3. (a) TEM image of KB&CTGU-15(1:2); (b,d) HRTEM image of KB&CTGU-15(1:2); (c,e) TEM-EDS mapping images of KB&CTGU-15(1:2).

XPS spectrum suggests that KB&CTGU-15(1:2) contains Ni, C, O, and N species (Figure S10).

To gain insight into the electrode kinetics of the studied catalysts for MOR, the charge transfer resistances (R_{ct}) of all catalysts were assessed. Figure 4a presents the EIS Nyquist plots for five catalysts at the onset potential. It was found that the R_{ct} of the KB&CTGU-15(1:2) (90 Ω) sample is much smaller than those of other composites such as KB&CTGU-15(1:1) (120 Ω), (KB&CTGU-15(1:3) (190 Ω)), (KB&CTGU-15(1:4) (209 Ω)) and pure CTGU-15 (358 Ω). This indicates highly efficient electron transport and favor-

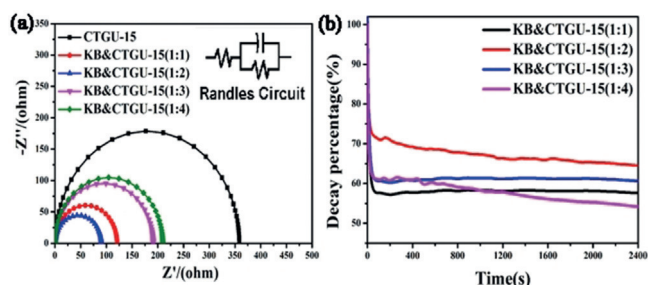


Figure 4. (a) Nyquist plots of EIS for CTGU-15 and composites; the inset shows the equivalent circuit. (b) Chronoamperograms of different catalysts.

able MOR kinetics at the KB&CTGU-15(1:2) electrolyte interface.

Finally, chronoamperometry was also used to further evaluate the durability and long-term activity of hybrid electrocatalysts for MOR. Figure 4b shows the chronoamperometric curves in 0.1M KOH solution containing 1.0M CH₃OH at a potential step of 0.6 V for 2400 s. Clearly, the current densities sharply dropped at the beginning and then slightly decreased for all four electrodes. At the beginning of the reaction, it is a fast kinetic reaction, so the active sites are free of adsorbed methanol molecules. The adsorption of more methanol molecules depends on the liberation of the electrocatalytic sites via methanol oxidation or of the intermediate species during MOR process. Therefore, the slightly decreased current density might be due primarily to the poisoning of the catalysts. These curves show that composites of CTGU-15 with KB sustain more stable current over time that is, 57.0% for KB&CTGU-15(1:1), 65.0% for KB&CTGU-15(1:2), 61.0% for KB&CTGU-15(1:3), and 54.0% for KB&CTGU-15(1:4). As expected, the current density for KB&CTGU-15(1:2) is the highest among these catalysts, which indicates its catalytic durability toward methanol electro-oxidation. The enhanced stability for KB&CTGU-15(1:2) might be due to the improved electron conduction between the CTGU-15 and KB. Some additional characterizations such as PXRD, XPS, SEM, and TEM testified to the robustness of CTGU-15 after MOR. The PXRD pattern in Figure S19 recorded after MOR indicates that the CTGU-15 sample is stable. XPS measurements of CTGU-15 before and after MOR were also assessed (Figure S20). The Ni2p spectra recorded both before and after catalysis show two characteristic peaks with binding energies about 870 and 855 eV. There were no significant changes in the Ni2p peaks before and after catalysis, suggesting that the chemical and structural environment is retained. Meanwhile, the SEM measurements indicate that the CTGU-15 catalyst retains its morphology during the MOR process (Figure S21). The TEM images obtained of CTGU-15 before (Figure S22a,b) and after catalysis (Figure S22d,e) are similar. The SAED pattern of post-catalysis CTGU-15 (Figure S22f) is very close to that of the pre-catalysis sample (Figure S22c). These results suggest that CTGU-15 retains the nature of the original crystalline state after MOR.

In summary, a new type of 3D porous material containing cubane [M₄(OH)₄] (M = Ni, Co) clusters has been prepared and structurally characterized. The electrocatalytic applications for MOR with the Ni form and its composites were evaluated. The as-prepared KB&CTGU-15(1:2) hybrid sample exhibit optimal electrocatalytic MOR activity compared to the pure Ni-MOF electrocatalyst. This enhanced performance toward MOR could be attributed to the unique active cubane [Ni₄(OH)₄] unit and possible synergetic effects of ketjen black and Ni-MOF. These results not only establish the composite between a microporous Ni-MOF and an electrical co-catalyst as an efficient and stable electrocatalyst for methanol oxidation reaction in alkaline media, but also demonstrate that the integration of transition-metal cubane [M₄(OH)₄] cluster into MOFs is a viable method to materials properties.

Acknowledgements

This work was supported by the NSF of China (Nos. 21673127, 21671119, 51572152, and 21805165), the Opening Project of Key Laboratory of Polyoxometalate Science of Ministry of Chinese Education, and the 111 Project of Hubei Province (2018-19-1).

Conflict of interest

The authors declare no conflict of interest.

Keywords: cluster compounds · electrocatalysis · methanol oxidation reaction · metal–organic frameworks

How to cite: *Angew. Chem. Int. Ed.* **2019**, *58*, 12185–12189
Angew. Chem. **2019**, *131*, 12313–12317

- [1] a) A. Badalyan, S. S. Stahl, *Nature* **2016**, *535*, 406–410; b) L. Huang, X. Zhang, Q. Wang, Y. Han, Y. Fang, S. Dong, *J. Am. Chem. Soc.* **2018**, *140*, 1142–1147; c) J. J. Mao, W. X. Chen, D. S. He, J. W. Wan, J. J. Pei, J. C. Dong, Y. Wang, P. F. An, Z. Jin, W. Xing, H. L. Tang, Z. B. Zhuang, X. Liang, Y. Huang, G. Zhou, L. Y. Wang, D. S. Wang, Y. D. Li, *Sci. Adv.* **2017**, *3*, e1603068.
- [2] A. Glösen, F. Dionigi, P. Paciok, M. Heggen, M. Müller, L. Gan, P. Strasser, R. E. Dunin-Borkowski, D. Stolten, *ACS Catal.* **2019**, *9*, 3764–3772.
- [3] a) T. Kwon, M. Jun, H. Y. Kim, A. Oh, J. Park, H. Baik, S. H. Joo, K. Lee, *Adv. Funct. Mater.* **2018**, *28*, 1706440; b) P. Yang, X. Yuan, H. Hu, Y. Liu, H. Zheng, D. Yang, L. Chen, M. Cao, Y. Xu, Y. Min, Y. Li, Q. Zhang, *Adv. Funct. Mater.* **2018**, *28*, 1704774; c) R. Rizo, R. M. Aran-Ais, E. Padgett, D. A. Muller, M. J. Lazaro, J. Solla-Gullon, J. M. Feliu, E. Pastor, H. D. Abruna, *J. Am. Chem. Soc.* **2018**, *140*, 3791–3797; d) L. Zhang, K. Doyle-Davis, X. Sun, *Energy Environ. Sci.* **2019**, *12*, 492–517.
- [4] B. Y. Xia, H. B. Wu, X. Wang, X. W. Lou, *J. Am. Chem. Soc.* **2012**, *134*, 13934–13937.
- [5] K. Zhu, X. Zhu, W. Yang, *Angew. Chem. Int. Ed.* **2019**, *58*, 1252–1265; *Angew. Chem.* **2019**, *131*, 1264–1277.
- [6] W. Yang, X. Yang, J. Jia, C. Hou, H. Gao, Y. Mao, C. Wang, J. Lin, X. Luo, *Appl. Catal. B* **2019**, *244*, 1096–1102.
- [7] B. Dong, W. Li, X. Huang, Z. Ali, T. Zhang, Z. Yang, Y. Hou, *Nano Energy* **2019**, *55*, 37–41.
- [8] a) D. Zhou, S. Wang, Y. Jia, X. Xiong, H. Yang, S. Liu, J. Tang, J. Zhang, D. Liu, L. Zheng, Y. Kuang, X. Sun, B. Liu, *Angew. Chem. Int. Ed.* **2019**, *58*, 736–740; *Angew. Chem.* **2019**, *131*, 746–750; b) L. Lv, Z. Yang, K. Chen, C. Wang, Y. Xiong, *Adv. Energy Mater.* **2019**, *9*, 1803358.
- [9] C. Wang, Y. Zhang, Y. Zhang, P. Xu, C. Feng, T. Chen, T. Guo, F. Yang, Q. Wang, J. Wang, M. Shi, L. Fan, S. Chen, *ACS Appl. Mater. Interfaces* **2018**, *10*, 9444–9450.
- [10] X. Cui, P. Xiao, J. Wang, M. Zhou, W. Guo, Y. Yang, Y. He, Z. Wang, Y. Yang, Y. Zhang, Z. Lin, *Angew. Chem. Int. Ed.* **2017**, *56*, 4488–4493; *Angew. Chem.* **2017**, *129*, 4559–4564.
- [11] a) Y. P. Wu, W. Zhou, J. Zhao, W. W. Dong, Y. Q. Lan, D. S. Li, C. Sun, X. Bu, *Angew. Chem. Int. Ed.* **2017**, *56*, 13001–13005; *Angew. Chem.* **2017**, *129*, 13181–13185; b) W. Li, S. Watzele, H. A. El-Sayed, Y. Liang, G. Kieslich, A. S. Bandarenka, K. Rodewald, B. Rieger, R. A. Fischer, *J. Am. Chem. Soc.* **2019**, *141*, 5926–5933; c) Z. Liang, C. Qu, D. Xia, R. Zou, Q. Xu, *Angew. Chem. Int. Ed.* **2018**, *57*, 9604–9633; *Angew. Chem.* **2018**, *130*, 9750–9780; d) B. Y. Xia, Y. Yan, N. Li, H. B. Wu, X. W. Lou, X. Wang, *Nat. Energy* **2016**, *1*, 15006; e) F. L. Li, Q. Shao, X. Huang, J. P. Lang, *Angew. Chem. Int. Ed.* **2018**, *57*, 1888–1892; *Angew. Chem.* **2018**, *130*, 1906–1910; f) D. Liu, J. Wan, G. Pang, Z. Tang, *Adv. Mater.* **2018**, 1803291; g) C. Cao, D. D. Ma, Q. Xu, X. T. Wu, Q. L. Zhu, *Adv. Funct. Mater.* **2018**, 1807418; h) W. Cheng, X. Zhao, H. Su, F. Tang, W. Che, H. Zhang, Q. Liu, *Nat. Energy* **2019**, *4*, 115–122.
- [12] W. H. Fang, L. Zhang, J. Zhang, *Chem. Soc. Rev.* **2018**, *47*, 404–421.
- [13] Y. Bai, Y. Dou, L. H. Xie, W. Rutledge, J. R. Li, H. C. Zhou, *Chem. Soc. Rev.* **2016**, *45*, 2327–2367.
- [14] Y. R. Wang, Q. Huang, C. T. He, Y. Chen, J. Liu, F. C. Shen, Y. Q. Lan, *Nat. Commun.* **2018**, *9*, 4466.
- [15] a) X. L. Wang, L. Z. Dong, M. Qiao, Y. J. Tang, J. Liu, Y. Li, S. L. Li, J. X. Su, Y. Q. Lan, *Angew. Chem. Int. Ed.* **2018**, *57*, 9660–9664; *Angew. Chem.* **2018**, *130*, 9808–9812; b) W. Zhou, D. D. Huang, Y. P. Wu, J. Zhao, T. Wu, J. Zhang, D. S. Li, C. Sun, P. Feng, X. Bu, *Angew. Chem. Int. Ed.* **2019**, *58*, 4227–4231; *Angew. Chem.* **2019**, *131*, 4271–4275; c) J. Q. Shen, P. Q. Liao, D. D. Zhou, C. T. He, J. X. Wu, W. X. Zhang, J. P. Zhang, X. M. Chen, *J. Am. Chem. Soc.* **2017**, *139*, 1778–1781.
- [16] D. I. Alexandropoulos, B. S. Dolinar, K. R. Vignesh, K. R. Dunbar, *J. Am. Chem. Soc.* **2017**, *139*, 11040–11043.
- [17] a) Y. B. Zhang, H. Furukawa, N. Ko, W. Nie, H. J. Park, S. Okajima, K. E. Cordova, H. Deng, J. Kim, O. M. Yaghi, *J. Am. Chem. Soc.* **2015**, *137*, 2641–2650; b) P. Guo, D. Dutta, A. G. Wong-Foy, D. W. Gidley, A. J. Matzger, *J. Am. Chem. Soc.* **2015**, *137*, 2651–2657.
- [18] a) F. Song, R. More, M. Schilling, G. Smolentsev, N. Azzaroli, T. Fox, S. Luber, G. R. Patzke, *J. Am. Chem. Soc.* **2017**, *139*, 14198–14208; b) L. Olshansky, R. Huerta-Lavorie, A. I. Nguyen, J. Vallapurackal, A. Furst, T. D. Tilley, A. S. Borovik, *J. Am. Chem. Soc.* **2018**, *140*, 2739–2742; c) A. I. Nguyen, K. M. Van Allsburg, M. W. Terban, M. Bajdich, J. Oktawiec, J. Amtawong, M. S. Ziegler, J. P. Dombrowski, K. V. Lakshmi, W. S. Drisdell, J. Yano, S. J. L. Billinge, T. D. Tilley, *Proc. Natl. Acad. Sci. USA* **2019**, *116*, 11630–11639.
- [19] A. I. Nguyen, L. E. Darago, D. Balcells, T. D. Tilley, *J. Am. Chem. Soc.* **2018**, *140*, 9030–9033.
- [20] C. Chen, Y. Chen, R. Yao, Y. Li, C. Zhang, *Angew. Chem. Int. Ed.* **2019**, *58*, 3939–3942; *Angew. Chem.* **2019**, *131*, 3979–3982.
- [21] J. Li, Q. Zhou, C. Zhong, S. Li, Z. Shen, J. Pu, J. Liu, Y. Zhou, H. Zhang, H. Ma, *ACS Catal.* **2019**, *9*, 3878–3887.
- [22] a) X. F. Lu, P. Q. Liao, J. W. Wang, J. X. Wu, X. W. Chen, C. T. He, J. P. Zhang, G. R. Li, X. M. Chen, *J. Am. Chem. Soc.* **2016**, *138*, 8336–8339; b) T. Ghosh, G. Maayan, *Angew. Chem. Int. Ed.* **2019**, *58*, 2785–2790; *Angew. Chem.* **2019**, *131*, 2811–2816; c) Z. Ji, C. Trickett, X. Pei, O. M. Yaghi, *J. Am. Chem. Soc.* **2018**, *140*, 13618–13622.
- [23] a) H. Furukawa, N. Ko, Y. B. Go, N. Aratani, S. B. Choi, E. Choi, A. Ö. Yazaydin, R. Q. Snurr, M. O’Keeffe, J. Kim, O. M. Yaghi, *Science* **2010**, *329*, 424; b) N. Klein, I. Senkovska, K. Gedrich, U. Stoeck, A. Henschel, U. Mueller, S. Kaskel, *Angew. Chem. Int. Ed.* **2009**, *48*, 9954–9957; *Angew. Chem.* **2009**, *121*, 10139–10142.
- [24] X. Zhao, X. Bu, E. T. Nguyen, Q. G. Zhai, C. Mao, P. Feng, *J. Am. Chem. Soc.* **2016**, *138*, 15102–15105.
- [25] Q. G. Zhai, X. Bu, X. Zhao, D. S. Li, P. Feng, *Acc. Chem. Res.* **2017**, *50*, 407–417.
- [26] X. Zhao, X. Bu, Q. G. Zhai, H. Tran, P. Feng, *J. Am. Chem. Soc.* **2015**, *137*, 1396–1399.

Manuscript received: June 7, 2019

Accepted manuscript online: July 8, 2019

Version of record online: August 5, 2019